Nanoparticle Inks for Directed Assembly of Three-Dimensional Periodic Structures**

By *Qi Li* and *Jennifer A. Lewis**

Nanoparticle assemblies may find potential application in photonic materials,[1] advanced ceramics,[2] electronics,[3] sensors,[4] and biological applications.[5] Several approaches have been developed to precisely position nanoparticles in both two-[2a,6] and three-dimensional[1b,c,7] (2D/3D) arrays. 2D nanoparticle arrays have been produced through self-assembly,[2a] DNA-mediated assembly,[6a,b] dip-pen nanolithography,[6c] and other lithographic techniques.[6d] 3D arrays have been created by self-assembly,[7a] layer-by-layer electrostatic-driven assembly[7b,c] or by nanoparticle infilling of colloidal crystals[1b,c] and other templates.[7d] Only this latter approach yields nanoparticle assemblies that exhibit periodicity in all three dimensions. While such assemblies are periodic at length scales on the order of colloidal dimensions, many targeted applications[2–5] require lattice constant(s) ranging from several micrometers to millimeters.

Direct-writing techniques,[8] such as robocasting,[8b] ink-jet printing,[8c] hot-melt printing,[8d] and micropen writing[8e] involve assembly via a layer-by-layer deposition of particle-based inks. Such techniques offer a powerful alternative for producing complex 3D structures, including space-filling solids and structures with high-aspect-ratio walls or spanning (unsupported) elements. The latter structure, which exhibits the desired 3D periodicity, places the most stringent demands on ink design. We recently demonstrated[9] that concentrated colloidal gels with tailored viscoelastic behavior could be used as inks to directly write 3D periodic structures with self-supporting features via robotic deposition (see Scheme 1). These micrometer-size colloidal inks could be used to fabricate structures with characteristic feature sizes of ~200 μm or higher. Difficulties, such as nozzle clogging, were encountered when attempting to create finer structures from colloidal inks.

Here, we develop concentrated nanoparticle inks for robotic deposition of 2D layers and 3D periodic structures with characteristic feature sizes of 100 μm or less. These inks must satisfy two important criteria.[9a] Firstly, they must exhibit a well-controlled viscoelastic response, i.e., they flow through the deposition nozzle and then "set" immediately to facilitate

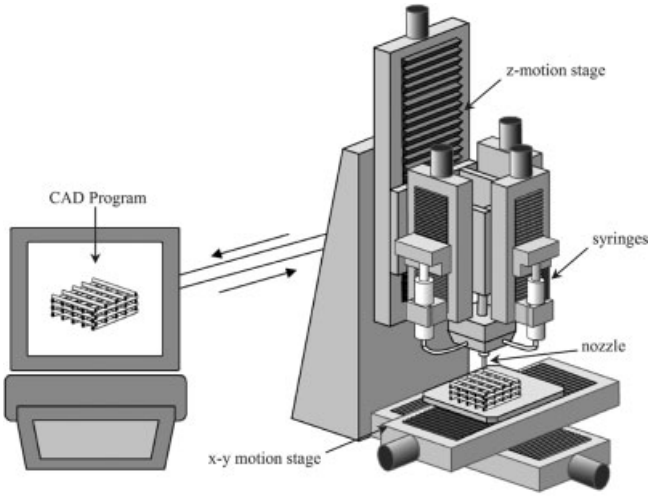

Scheme 1. Schematic illustration of the robotic deposition apparatus used in the directed assembly of concentrated nanoparticle inks. Inks are housed in individual syringe reservoirs mounted on the *z*-axis motion stage, and deposited through a cylindrical nozzle (diameter ranging from 30 μm to 100 μm) onto a moving *x*–*y* stage. Typical build times for the 3D periodic structures illustrated in subsequent figures are ~30 min/part at an *x*–*y* table speed of 1 mm s^{-1}. (Note: structures were assembled in a low viscosity oil reservoir (not shown) placed on the *x*–*y* stage to minimize drying during deposition.)

shape retention of the deposited features even as they span gaps in the underlying layer(s). Secondly, they must contain a high nanoparticle volume fraction to minimize drying-induced shrinkage after assembly is complete, i.e., the particle network is able to resist compressive stresses arising from capillary tension.[10] These criteria require careful control of interparticle forces to first generate a highly concentrated, stable dispersion followed by inducing a system change (e. g., ΔpH, ionic strength, or solvent quality) that promotes the fluid-to-gel transition illustrated schematically in Figure 1a.

We demonstrated this nanoparticle ink design with an aqueous system comprised of poly(acrylic acid) (PAA)-coated barium titanate ($BaTiO_3$) nanoparticles, whose interactions were carefully modulated by changing ionic strength through the addition of monovalent or divalent salt species. PAA is a linear polyelectrolyte that contains one carboxylic acid group per monomer unit along its backbone. PAA becomes negatively charged with these groups fully ionized under the experimental conditions of interest (~pH 9).[11] In contrast, the $BaTiO_3$ nanoparticles are positively charged under these conditions (see Fig. 1b).[12] Due to strong electrostatic attractions between oppositely charged species, PAA readily adsorbs onto the $BaTiO_3$ nanoparticles inducing a dramatic charge reversal. The negatively charged, PAA-coated nanoparticles are stable under low ionic strength, but rapidly aggregate in suspension under high-ionic-strength conditions.

In our approach, we first generated a well-dispersed $BaTiO_3$ suspension (pH 9) to facilitate the high solids loading (>45 %) required, followed by inducing a fluid-to-gel transition by adding monovalent or divalent salt species to generate the desired viscoelastic response. A dramatic rise in elastic properties accompanied this phase transition, as shown in Figure 1c. Both the shear yield stress and elastic modulus in-

[*] Prof. J. A. Lewis, Q. Li
Materials Science and Engineering Department
Frederick Seitz Materials Research Laboratory
NSF Center for Directed Assembly of Nanostructures
UIUC, Urbana, IL 61801 (USA)
E-mail: jalewis@staff.uiuc.edu

[**] The authors gratefully acknowledge the generous funding for this project provided by the NSF Center for Directed Assembly of Nanostructures (Grant # DMR 01-17792). The robotic deposition apparatus used in this work was designed and built by J. Cesarano and customized software for 3D fabrication was developed by J. E. Smay. J. A. Lewis acknowledges partial support from the U.S. Department of Energy, Division of Materials Sciences through the Frederick Seitz Materials Research Laboratory (Grant # DEFG02-91-ER45439).

 DOI: 10.1002/adma.200305413

ADVANCED MATERIALS

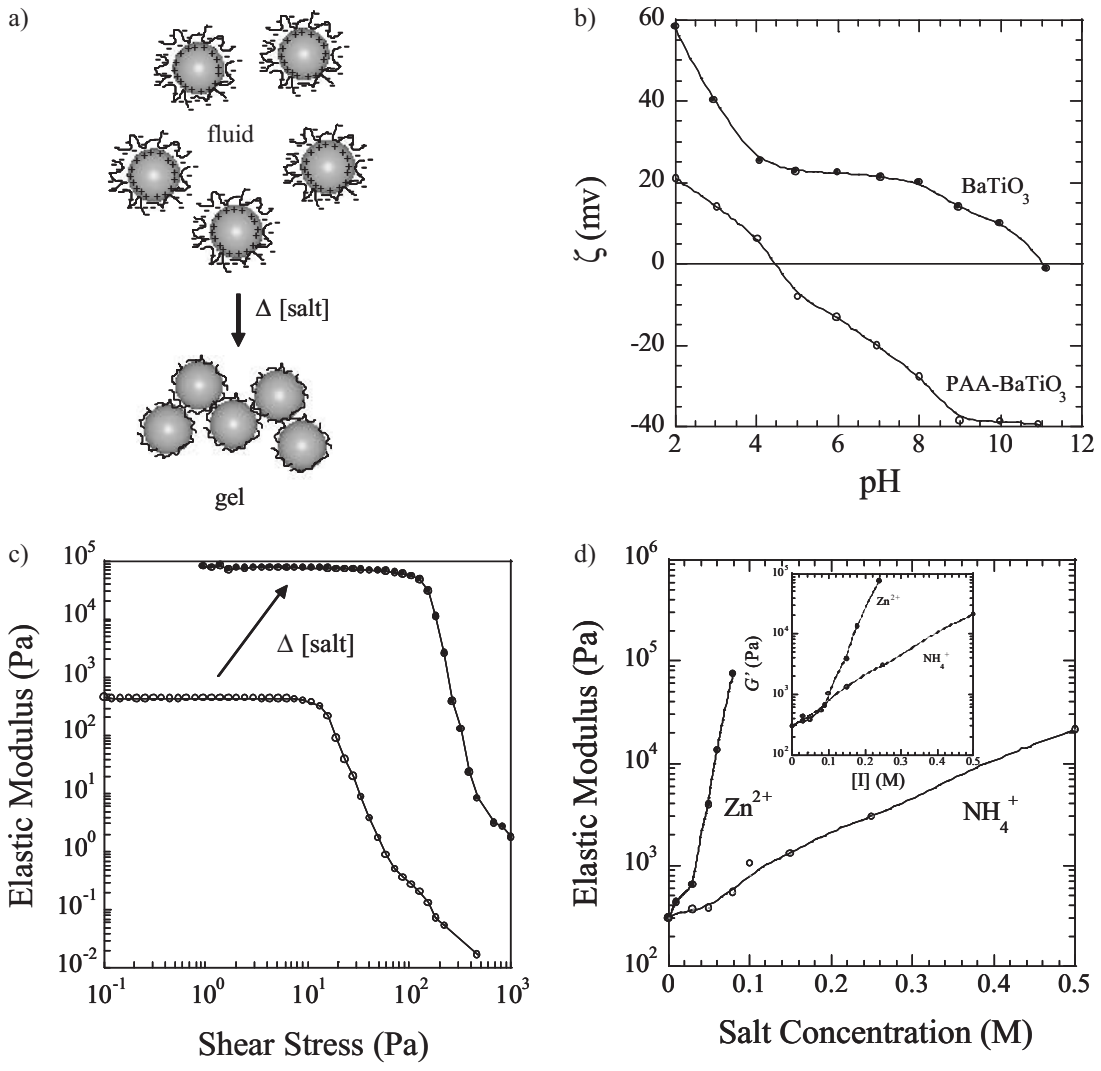

Fig. 1. a) Schematic illustration of the fluid-to-gel transition for $BaTiO_3$ nanoparticle inks that occurs upon increasing salt addition. b) Zeta potential of pure $BaTiO_3$ (closed symbols) and PAA-coated $BaTiO_3$ nanoparticles (open symbols) in suspension ($\phi = 0.1$) as a function of pH. c) Elastic modulus as a function of applied shear stress for 50 vol.-% $BaTiO_3$ nanoparticle inks with 0.01 M (open symbols) and 0.08 M (closed symbols) zinc acetate additions. d) Equilibrium elastic modulus of 50 vol.-% $BaTiO_3$ nanoparticle inks with monovalent (open symbols) and divalent (closed symbols) salt additions (Note: Inset plot illustrates G' as a function of ionic strength for these inks.).

creased by an order of magnitude (or more) due to strengthened interparticle attractions,[13] as given by the following scaling relationship:[14]

$$y = k\left(\frac{\phi}{\phi_{gel}} - 1\right)^x \quad (1)$$

where y is the elastic property of interest (shear yield stress (τ_y) or elastic modulus (G')), k is a constant, ϕ_{gel} is the nanoparticle volume fraction at the gel point, and x is the scaling exponent (~2.5). The equilibrium mechanical properties of nanoparticle gels are governed by two parameters: ϕ, which is proportional to their bond density, and ϕ_{gel}, which scales inversely with bond strength. Because interparticle attractions intensify with increasing salt concentration, nanoparticle gels (of constant ϕ) experienced significant increases in their elastic properties (see Fig. 1).

Interestingly, the $BaTiO_3$ nanoparticle inks exhibited significant differences in elasticity in the presence of mono- or divalent salt species (see Fig. 1d). For example, at an equivalent salt concentration of 0.1 M, the elastic modulus was nearly two orders of magnitude higher for inks containing divalent salt compared to those with monovalent salt additions. If one accounts for differences in ionic strength—

$$[I] = \frac{1}{2}\sum_i n_i Z_i^2 \quad (2)$$

where n_i is the concentration of ion i, Z_i is the charge of ion i—by plotting the G' values as a function of [I], then two trends emerge (see inset, Fig. 1d). At low [I] (≤0.1 M), the ink elasticity is independent of the counterion valency (i.e., NH_4^+ or Zn^{2+}) at a given value of [I]. However, at higher [I] values (>0.1 M), G' rises more sharply for inks containing

divalent salt additions. Our observations reflect interactions between oppositely charged ions (counterions) in solution and PAA-coated $BaTiO_3$ nanoparticles. Unlike monovalent counterions (e.g., NH_4^+) that only "screen" negatively charged COO^- groups, divalent counterions (e.g., Zn^{2+}) can also promote aggregation through "ion-bridging" effects between charged PAA chains adsorbed on different nanoparticles in suspension.[15] The screening effects observed at low ionic strength lead to a substantially reduced adsorbed layer thickness.[16] Under such conditions, long-range van der Waals interactions dominate the bonding between nanoparticles in the ink. The observed differences in ink elasticity at higher ionic strengths likely stem from a cross-over from purely van der Waals dominated interactions to ion bridging effects that further intensify bonding between nanoparticles within the gel network.

Concentrated nanoparticle gels (pH 9, $[Zn^{2+}] = 0.06$ M) were utilized as inks for directed assembly of 2D layers and 3D periodic structures, as shown in Figures 2 and 3, respectively. This salt concentration was utilized because it produced nanoparticle inks that exceeded the minimum elasticity, $G' \sim 10^4$ Pa, required to produce the 3D spanning features of interest (see Smay et al.).[9a] It is noteworthy that roughly an order of magnitude higher salt concentration would be required, if monovalent salt additions were used to generate the desired network strength. This gel-based ink was robotically deposited onto a moving x–y stage yielding a 2D pattern (see Scheme 1). After a given layer was generated, the stage was incremented in the z-direction (Δz) and another layer was deposited. This process was repeated to yield 3D structures. The ink flowed through a cylindrical nozzle at the volumetric flow rate required to maintain a constant deposition speed (v) of 1 mm s^{-1}. As the ink exits the nozzle, it forms a continuous, rod-like filament with a rigid (gel) core-fluid shell architecture that simultaneously promotes shape retention while allowing the rods to fuse together at their contact points.[9a] This filamentary architecture arises because the percolating network of attractive particles within the gelled ink is capable of transmitting stress above ϕ_{gel}. When stressed beyond its yield point (τ_y), the ink exhibits shear thinning flow behavior due to the attrition of particle–particle bonds within the gel, as described by:[17]

$$\tau = \tau_y + K\dot{\gamma}^n \quad (3)$$

where τ is the shear stress, n is the shear-thinning exponent (< 1), K is the viscosity parameter, and $\dot{\gamma}$ is the shear rate. This behavior is reflected in the rheological response shown in Figure 1c. Below τ_y, G' is independent of applied stress (i.e., the system resides in the linear viscoelastic region). Above τ_y, interparticle bonds rupture leading to a sharp decrease in G' needed to facilitate flow. To maintain constant ink composition (ϕ) and, thus, prevent changes in ink rheology due to water evaporation during assembly, the deposition process was carried out in an oil reservoir. The 2D layers and 3D structures were removed from this reservoir after assembly was completed and then dried under ambient conditions.

2D layers consisting of a continuous spiral pattern and a parallel array of rods were produced, as shown in Figs. 2a,b,

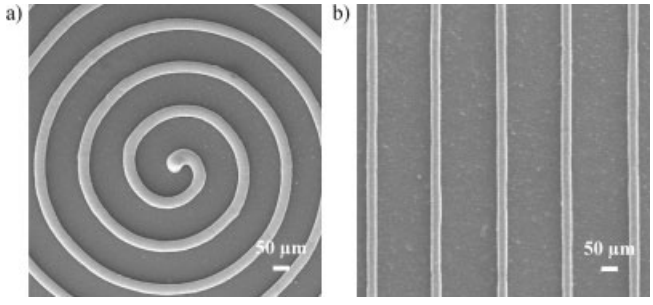

Fig. 2. SEM images of 2D layers assembled from concentrated $BaTiO_3$ nanoparticle inks deposited through a 30 μm nozzle: a) Spiral pattern ($D = 30$ μm) with an increasing radius $R = a\phi$ ($a = 150$ μm/2π, and ϕ is the increasing angle) and b) parallel array of rods ($D = 30$ μm) with an inter-rod spacing, d, of 200 μm.

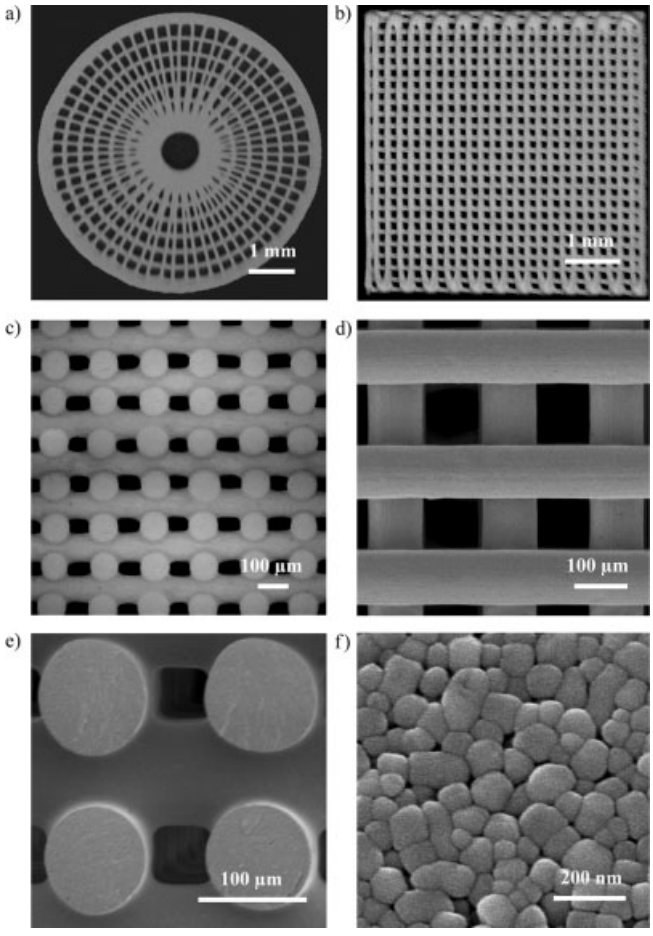

Fig. 3. Optical images (top view) of a) 3D radial array and b) 3D periodic lattice assembled from concentrated $BaTiO_3$ nanoparticle inks deposited through a 100 μm nozzle. c) Optical image (cross-sectional view) of the 3D periodic lattice shown in (b). SEM images of the 3D periodic lattice shown in (b), where (d,e) illustrate top and cross-sectional views of the lattice at higher magnification, and (f) illustrates the $BaTiO_3$ nanoparticle network that comprises these structures after drying.

ADVANCED MATERIALS

respectively. We encountered difficulties with nozzle clogging at this feature size (nozzle diameter = 30 μm), which inhibited the assembly of subsequent layers. We attribute this phenomenon to pressure filtration within the nozzle, and experiments are now underway to understand the dynamic processes that occur during ink deposition. To create the 3D periodic structures shown in Figure 3, we utilized a larger nozzle diameter ($D = 100$ μm). Ink deposition through nozzles of intermediate size (30 μm < D < 100 μm) was not explored due to the absence of commercially available nozzles. Both radial arrays and simple tetragonal lattices were produced with ease. Optical images (Figs. 3a–c) reveal an annular symmetry for radial arrays and a tetragonal symmetry for 3D lattices. The radial arrays were created via the sequential deposition of layers with alternating patterns of concentric rings and a circular array of oriented rods. The concentric rings maintained their circular shape despite the changing arc length between supports provided by the radial lines in the underlying layer (Fig. 3a). Top and cross-section views (Figs. 3b,c) of 3D lattices depict the cylindrical nature of the rods and their high degree of regularity. The average center-to-center spacing between rods along the x-axis (or y-axis) is 188 ± 4.6 μm, and along the z-axis is 160 ± 3.6 μm, respectively. The observed difference between the in-plane and z-spacing ($\bar{z}/\bar{x} = 0.85$) arises from the building conditions utilized to promote strong bonding between rods, i.e., $\Delta z \sim 0.9\,D$. Scanning electron microscopy (SEM) images of the simple tetragonal lattice (Figs. 3d,e) reveal their smooth exterior surfaces and cylindrical features, which are preserved during the assembly and drying process. A higher magnification view (Fig. 3f) of a representative rod surface reveals the dense nanoparticle assembly created upon drying.

In summary, we have developed concentrated nanoparticle inks with the appropriate viscoelastic response to enable direct-write assembly of 2D layers and 3D periodic structures with fine feature sizes of ~30 μm and 100 μm, respectively. This approach opens up an unexplored avenue for engineering complex 3D structures from nanoparticle building blocks, which may be relevant for a broad range of technological applications.

Experimental

Concentrated $BaTiO_3$ nanoparticle dispersions were prepared by first adding an appropriate amount (0.6 mg PAA/m^2 $BaTiO_3$) of PAA ($M_w = 5000$ g mol^{-1}, Polyscience Inc., Warrington, PA) to deionized water at pH 9. PAA, a weakly charged anionic polyelectrolyte, served as a dispersant. All pH adjustments were made using certified 1.0 N NH_4OH and HNO_3 (Fisher Scientific). An appropriate amount of $BaTiO_3$ nanoparticles (mean radius, $a = 30$ nm and size range from a ~ 15–60 nm, $\rho = 5.82$ g cm^{-3}, and specific surface area of 15.6 m^{2}g^{-1}; BT-16 K-Plus, Cabot Co., Boyertown, PA) were then added to the solution. The suspension was sonicated (Model 550 Sonic Dismembrator; Fisher Scientific, Pittsburgh, PA) for 5 min with a 1 s on/off pulse sequence at 20 kHz. The pH was then readjusted to 9, and the suspension was allowed to magnetically stir for 24 h. This procedure created a uniform dispersion of $BaTiO_3$ nanoparticles in suspension, which was then filtered through 20 μm and 5 μm filters to eliminate any large agglomerates. The suspension was then centrifuged at 2500 revolutions per minute (rpm) for 1 h. After centrifuging, the supernatant was decanted and the sediment was redispersed to create a concentrated nanoparticle suspension ($\phi \sim 0.5$). An appropriate amount of ammonium chloride or zinc acetate was added to tailor interparticle interactions to induce the desired fluid-to-gel transition. It should be noted that the addition of alternate monovalent or divalent salt species yielded similar behavior. The ammonium chloride (5 M) or zinc acetate (1 M) stock solutions were prepared by dissolving NH_4Cl or $Zn(C_2H_3O_2)_2{\cdot}2H_2O$ (Fisher Chemicals, Fair Lawn, NJ) in deionized water. The resulting nanoparticle gel was homogenized, an aliquot of cellulose (Methocel F4M; Dow Chemical Co., Midland, MI) stock solution was added to yield a final cellulose concentration of 5 mg mL^{-1}, and the gel was once again homogenized by high-shear agitation. Cellulose acted as a thickening agent thereby increasing the solution viscosity from ~ 1 mPa s to 30 mPa s, which served to reduce flocculation kinetics. This allowed the rigid core-fluid shell architecture of the deposited filaments to persist facilitating rod–rod adhesion during assembly [9a].

Zeta-potential (ζ) measurements (ESA 9800 apparatus; Matec Applied Science, Northboro, MA) were carried out on a pure $BaTiO_3$ and PAA-$BaTiO_3$ suspensions ($\phi = 0.1$) as a function of pH.

Concentrated nanoparticle gels ($\phi \sim 0.5$) were prepared for rheological characterization and robotic deposition following the procedure outlined above, which yielded gels of varying strength depending on the salt concentration and valency. The shear elastic modulus (G') and yield stress (τ_y) were measured using a controlled stress rheometer (Bohlin CVOR-200 apparatus, Cranbury, NJ) fitted with a concentric cylinder geometry (C-14). The C-14 bob was roughened with periodic grooves to mitigate possible wall-slip effects [18]. Oscillatory measurements were carried out at 1 Hz and a stress sweep was performed in ascending order. Prior to each measurement, a pre-shear of 200 s^{-1} was applied for 300 s followed by a 7200 s equilibration time to ensure a uniform shear history and that the suspension had reached equilibrium. All measurements were carried out at a constant temperature of 22 °C.

2D layers, 3D radial arrays, and 3D periodic lattices were fabricated using a robotic deposition apparatus (JL2000 apparatus, Robocasting Enterprises, Inc., Albuquerque, NM). This directed assembly technique employs an ink-delivery system mounted on a z-axis motion control stage for agile printing onto a moving x–y stage. The 3-axis motion of the x–y and z-stages was independently controlled by a custom-designed, computer-aided program (RoboCAD 2.0) that allowed for the construction of any 2D pattern, from which complex, 3D architectures could be created in a layerwise build sequence. The 2D layers consisted of a spiral pattern ($D = 30$ μm) with an increasing radius $R = a\varphi$ ($a = 150$ μm/2π, and φ is the increasing angle) and a parallel array of rods ($D = 30$ μm) with an inter-rod spacing, d, of 200 μm. The ink was housed in a syringe (barrel diameter = 4.6 mm, EFD Inc., East Providence, RI) and deposited through a tapered glass microtip ($D = 30$ μm) at a volumetric flow rate ($= 0.25\,\pi D^2 v$) required to maintain a constant x–y table speed (v) of 1 mm s^{-1}.

3D radial arrays consisted of sequential deposition of layers with alternating patterns of concentric rings and a circular array of oriented rods. The first layer was an array of seven equally spaced concentric rings between an inner and outer diameter of 0.5 and 3.0 mm, respectively. In the second layer, an array of radially oriented rods was deposited between the inner and outer radii. The angular spacing between the rods was 5.714°, so the arc length between adjacent rods varied from 300 μm to 25 μm moving from the outer to inner radius. 3D lattice structures consisted of a linear array of rods aligned with the x or y-axis such that their orientation was orthogonal to the previous layer with a center-to-center rod spacing (d) of 200 μm. To promote intimate contact between layers, a layer spacing Δz of $0.9\,D$ was used in the fabrication process. The ink was housed in the syringe described above and deposited through a chamfer nozzle ($D = 100$ μm) at a volumetric flow rate ($= 0.25\,\pi D^2 v$) required to maintain a constant x–y table speed (v) of 1 mm s^{-1}. Each deposition process was carried out under a non-wetting oil to prevent drying during assembly. After assembly, structures were removed from the oil bath and dried under ambient conditions, where they experienced ~ 1 % linear shrinkage. Note, the dried structures could be removed from the substrate and fully densified at elevated temperatures (~ 1150 °C) without cracking.

Optical images of the dried structures were taken by a DCS 330 Digital Camera (Kodak). SEM images were obtained with a Hitachi S-4700 Scanning Electron Microscope (Hitachi Ltd., Tokyo, Japan). After fabrication and drying, structures were mounted and sputtered with gold for 1 min (Emitech K575 Sputter Coater, Emitech Ltd., Ashford Kent, UK) prior to imaging.

Received: May 19, 2003
Final version: June 24, 2003

[1] a) E. Chow, S. Y. Lin, S. G. Johnson, P. R. Villeneuve, J. D. Joannopoulos, J. R. Wendt, G. A. Vawter, W. Zubrzycki, H. Hou, A. Alleman, *Nature* **2000**, *407*, 983. b) O. D. Velv, P. M. Tessier, A. M. Lenhoff, E. W. Kaler, *Nature* **1999**, *401*, 548. c) D. Wang, V. S. Maceira, L. M. Liz-Marzán, F. Caruso, *Adv. Mater.* **2002**, *14*, 908.

[2] a) H. Zeng, J. Li, J. P. Liu, Z. L. Wang, S. Sun, *Nature* **2002**, *420*, 395. b) J. E. Smay, J. Cesarano III, B. A. Tuttle, J. A. Lewis, *J. Appl. Phys.*

2002, *92*, 6119. c) F. Tressler, S. Alkoy, A. Dogan, R. E. Newnham, *Composites: Part A* **1999**, *30*, 477. d) M. P. Rao, A. J. Sanchez-Herencia, G. E. Beltz, R. M. McMeeking, F. F. Lange, *Science* **1999**, *286*, 102.

[3] a) R. P. Andres, T. Bein, M. Dorogi, S. Feng, J. I. Henderson, C. P. Kubiak, W. Mahoney, R. G. Osifchin, R. Reifenberger, *Science* **1996**, *272*, 1323. b) U. Simon, *Adv. Mater.* **1998**, *10*, 1487.

[4] a) R. Elghanian, J. J. Storhoff, R. C. Mucic, R. L. Letsinger, C. A. Mirkin, *Science* **1997**, *277*, 1078. b) J. M. Perez, T. O'Loughin, F. J. Simeone, R. Weissleder, L. Josephson, *J. Am. Chem. Soc.* **2002**, *124*, 2856.

[5] a) E. Dujardin, S. Mann, *Adv. Mater.* **2002**, *14*, 775. b) T.-M. Chu, J. Halloran, S. J. Hollister, S. E. Feinburg, *J. Mater. Sci.: Mater. Med.* **2001**, *12*, 471.

[6] a) C. A. Mirkin, R. L. Letsinger, R. C. Mucic, J. J. Storhoff, *Nature* **1996**, *382*, 607. b) A. P. Alivisatos, K. P. Johnsson, X. Peng, T. E. Wilson, C. J. Loweth, M. Bruchez, P. G. Schultz, *Nature* **1996**, *382*, 609. c) X. Liu, L. Fu, S. Hong, V. P. Dravid, C. A. Mirkin, *Adv. Mater.* **2002**, *14*, 231. d) F. Hua, T. H. Cui, Y. Lvov, *Langmuir* **2002**, *18*, 6712.

[7] a) Y. Lin, H. Skaff, T. Emrick, A. D. Dinsmore, T. P. Russell, *Science* **2003**, *299*, 226. b) R. Iler, *J. Colloid Interface Sci.* **1966**, *21*, 569. c) E. R. Kleinfeld, G. S. Ferguson, *Science* **1994**, *265*, 370. d) S. A. Davis, M. Breulmann, K. H. Rhodes, B. Zhang, S. Mann, *Chem. Mater.* **2001**, *13*, 3218.

[8] a) D. B. Chrisey, *Science* **2000**, *289*, 879. b) J. Cesarano III, P. Calvert, *US Patent 6 027 326*, **2000**. c) J. H. Song, M. J. Edirisinghe, J. R. G. Evans, *J. Am. Ceram. Soc.* **1999**, *82*, 3374. d) K. A. M. Seerden, N. Reis, J. R. G. Evans, P. S. Grant, J. W. Halloran, B. Derby, *J. Am. Ceram. Soc.* **2001**, *84*, 2514. e) S. L. Morissette, J. A. Lewis, P. G. Clem, J. Cesarano III, D. B. Dimos, *J. Am. Ceram. Soc.* **2001**, *84*, 2462.

[9] a) J. E. Smay, J. Cesarano III, J. A. Lewis, *Langmuir* **2002**, *18*, 5429. b) J. E. Smay, G. M. Gratson, R. F. Shepherd, J. Cesarano III, J. A. Lewis, *Adv. Mater.* **2002**, *14*, 1279.

[10] J. J. Guo, J. A. Lewis, *J. Am. Ceram. Soc.* **1999**, *82*, 2345.

[11] V. Hackley, *J. Am. Ceram. Soc.* **1997**, *80*, 2315.

[12] U. Paik, V. Hackley, *J. Am. Ceram. Soc.* **2000**, *83*, 2381.

[13] J. A. Lewis, *J. Am. Ceram. Soc.* **2000**, *83*, 2341.

[14] G. M. Channell, C. F. Zukoski, *AIChE J.* **1997**, *43*, 1700.

[15] a) F. J. Solis, M. Olvera de la Cruz, *J. Chem. Phys.* **2000**, *112*, 2030. b) J. X. Tang, P. A. Janmey, *J. Biol. Chem.* **1996**, *271*, 8556. c) E. Raspaud, M. Olvera de la Cruz, J.-L. Sikorav, F. Livolant, *Biophys. J.* **1998**, *74*, 381. d) J. M. Berg, P. M. Claesson, R. D. Newman, *J. Colloid Interface Sci.* **1993**, *161*, 182.

[16] a) S. Biggs, T. W. Healy, *J. Chem. Soc. Faraday Trans.* **1994**, *90*, 3415. b) N. S. Bell, J. Sindel, F. Aldinger, W. M. Sigmund, *J. Colloid Interface Sci.* **2002**, *254*, 296.

[17] W. H. Herschel, R. Bulkley, *Kolloid Z.* **1926**, *39*, 291.

[18] R. Buscall, J. I. McGowan, A. J. Morton-Jones, *J. Rheol.* **1993**, *37*, 621.

Self-Assembled Electroluminescent Polymers Derived from Terpyridine-Based Moieties**

By *Sze-Chit Yu*, *Chi-Chung Kwok*, *Wai-Kin Chan*, and *Chi-Ming Che**

The discovery that poly(phenylenevinylene) (PPV) and its derivatives[1] exhibit electroluminescence (EL) has provided new impetus to the development of polymeric light-emitting devices (PLEDs). Polymers are promising materials for LEDs due to their color tunability, anisotropic light emission, and synthetic versatility. By using simple spin-coating or ink-jet printing methods,[2] large-area devices can be fabricated. However, the practical applicability of presently known functional polymers such as PPV, poly(*p*-phenylene) (PPP), polythiophene (PT), and polyfluorene (PFO) is limited by their oxidative stabilities and/or electronic properties. Although PPV-based materials demonstrate high PL and EL efficiencies and their emission energies are tunable, they usually suffer from photooxidative degradation upon incorporation into EL devices.[3] Applications of PPP are limited by its low solubility. PT and related derivatives have been shown to display EL from the blue to the near-infrared region with low quantum efficiencies. PFO is a blue-light-emitting material that shows good thermal stability and high EL quantum efficiency, but chain aggregation and keto-defect sites in the polymer can cause degradation of EL devices.[4,5] Light-emitting polymers present technical problems in the fabrication of LEDs, including color impurity, imbalanced charge injection, and low EL efficiencies.[5]

The use of transition or rare earth metal complexes for organic LEDs has attracted much attention recently because of the enhancement in EL efficiency by utilizing energy from the triplet excited state.[6] Chan and co-workers demonstrated that incorporation of ruthenium bipyridyl complexes into conjugated polymers enhances the charge carrier mobilities.[7] Through attachment of different transition metal complexes onto polymer chains, tuning of light-emitting properties could be achieved.[8] 2,2′:6′,2″-Terpyridine is known to have a high binding affinity toward divalent and trivalent metal ions to form octahedral complexes.[9,10] Dobrawa and Würthner recently reported a strong red light-emitting polymer composed of perylene bisimide dye fragments connected to bis(terpyridyl)zinc(II) moieties.[10] Using the Zn^{2+} ion as a template to assemble organic building blocks into polymer chains through coordination to chelating terpyridyl units is an appealing strategy for the construction of photoluminescent metal-containing polymers with well-defined structures. Such zinc(II)-containing polymers have the potential to become high-performance emissive or host materials in electroluminescent devices. Herein we report the synthesis of a family of self-assembled zinc terpyridyl polymers, which exhibit emission ranging in color from violet to yellow and high PL quantum yields.

Scheme 1 depicts the synthetic procedures for polymers **2a**–**i** and model compound **3b** respectively. For **2a**–**e**, the spacer units R have flexible $-CH_2-$ or ester linkages, while for **2f**–**i**, the rigid backbone is derived from conjugated phenylene groups. In contrast to other polymerization methods such as the Wittig[11] or Heck coupling reactions,[12] the present procedure requires no catalyst. The kinetic lability of Zn^{2+} and the stability of the six-coordinate bis(terpyridyl)zinc(II) moiety allows the self-assembly reaction to take place under mild conditions. Yields of up to 80 % were obtained for the polymers. The physical properties are summarized in Table 1. The inherent viscosities range from 0.48 to 1.21 dL g^{-1}, as determined using an Ubbelohde viscometer in *N*-methylpyrrolidinone

[*] Prof. C.-M. Che, Dr. S.-C. Yu, C.-C. Kwok, Dr. W.-K. Chan
Department of Chemistry and
HKU-CAS Joint Laboratory on New Materials
University of Hong Kong
Pokfulam Road, Hong Kong SAR (China)
E-mail: cmche@hku.hk

[**] This work was supported by The University of Hong Kong, Innovation and Technology Commission of Hong Kong Special Administrative Region (HKSAR), China (Project No. ITS/53/01) and Research Grants Council of The HKSAR, China (Project No. HKU 7096/00P).

 DOI: 10.1002/adma.200305002